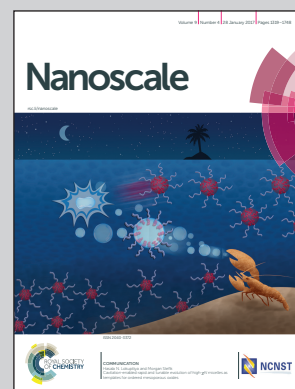


Showcasing research from the Institute for Translational Nanomedicine, Shanghai East Hospital, The Institute for Biomedical Engineering and Nano Science, Tongji University School of Medicine, Shanghai, and The Materials Science and Engineering Program, Department of Mechanical and Materials Engineering, College of Engineering and Applied Science, University of Cincinnati, Ohio, USA.

Biomarkerless targeting and photothermal cancer cell killing by surface-electrically-charged superparamagnetic  $\text{Fe}_3\text{O}_4$  composite nanoparticles

Without any biomarkers, cancer cells are specifically targeted based on the surface electrical charge differences between the cells and  $\text{Fe}_3\text{O}_4$  nanoparticles. The cancer cell targeting and binding by the positively charged  $\text{Fe}_3\text{O}_4$  is selective and specific only on negatively charged cancer cells, regardless of their phenotype. A laser is applied simultaneously to induce the photothermal effect of  $\text{Fe}_3\text{O}_4$  for the instant killing of cancer cells due to the intimate contacts between the nanoparticles and the cell surfaces.

As featured in:



See Yilong Wang, Donglu Shi et al., *Nanoscale*, 2017, 9, 1457.



[rsc.li/nanoscale](http://rsc.li/nanoscale)

Registered charity number: 207890



Cite this: *Nanoscale*, 2017, 9, 1457

## Biomarkerless targeting and photothermal cancer cell killing by surface-electrically-charged superparamagnetic Fe<sub>3</sub>O<sub>4</sub> composite nanoparticles†

Xiao Han,<sup>a,b</sup> Zicheng Deng,<sup>a,b</sup> Zi Yang,<sup>a,b</sup> Yilong Wang,<sup>\*b</sup> Huanhuan Zhu,<sup>b</sup> Bingdi Chen,<sup>b</sup> Zheng Cui,<sup>b,c</sup> Rodney C. Ewing<sup>d</sup> and Donglu Shi<sup>\*b,e</sup>

A major challenge in cancer therapy is localized targeting of cancer cells for maximum therapeutic effectiveness. However, due to cancer heterogeneities, the biomarkers are either not readily available or specific for effective targeting of cancer cells. The key, therefore, is to develop a new targeting strategy that does not rely on biomarkers. A general hallmark of cancer cells is the much increased level of glycolysis. The loss of highly mobile lactate from the cytoplasm inevitably removes labile inorganic cations to form lactate salts and acids as part of the lactate cycle, creating a net of negative surface charges. This net of negative charges on cancer cell surfaces biophysically distinguishes themselves from normal cells. In this study, cancer cells are targeted by using positively-charged, fluorescent, superparamagnetic Fe<sub>3</sub>O<sub>4</sub>-composite nanoparticles. The positively-charged Fe<sub>3</sub>O<sub>4</sub> composite nanoparticles bind predominantly to cancer cells due to their negatively-charged surfaces. Upon electrical-charge-mediated Fe<sub>3</sub>O<sub>4</sub> nanoparticle binding onto cancer cells, irradiation by using an 808 nm laser is subsequently applied to induce photothermal hyperthermia that kills the cancer cells directly. The negatively-charged composite nanoparticles are found, however, not to target and bind the cancer cells due to the electrostatic repulsive force between them. This unique strategy paves a new path for effective targeting and direct cancer cell killing without relying on any biomarkers and anticancer drugs.

Received 9th September 2016,  
Accepted 17th November 2016

DOI: 10.1039/c6nr07161a

[www.rsc.org/nanoscale](http://www.rsc.org/nanoscale)

## Introduction

There is an increasing need for early diagnosis of cancer, prior to the detection of anatomic anomalies.<sup>1–6</sup> An important advancement in cancer diagnosis is to locally recognize cancer cells at the molecular level with highly specific biomarkers for maximum therapeutic benefit.<sup>1</sup> With the current approaches, cancer-specific ligands are required and conjugated on nano-

vectors for targeted delivery to tumor sites.<sup>7–11</sup> This conventional strategy has been limited due to two major issues: (i) unavailability of biomarkers for many cancer phenotypes, and (ii) biomarker non-specificity to respective cancer cells. The current cancer research has focused on identifying biomarkers that are specific to a particular cell phenotype.<sup>12</sup> However, it is theoretically impossible for any molecule to be present at a significant level on cancer cells of all types, but be completely absent on normal cells.<sup>3–5</sup> For instance, extensive efforts have been devoted to screening biomarkers and the corresponding ligands, but only a few cancer targeting sites such as HER2 and PSMA are recognized for early detection or targeted therapy of breast cancer and prostate cancer, respectively.<sup>13,14</sup> In some cases, the overexpression of folate and transferrin receptors, associated with the increased nutritional uptake of malignant tumors, has also been used for targeting, but with limited success.<sup>15,16</sup> Passive targeting has been another possible approach for cancer targeting therapy. Among them, the enhanced permeability and retention (EPR) effect and magnetically-driven targeting have been extensively studied.<sup>17–19</sup> In passive targeting, the long circulation time of the nano therapeutics can result in adverse effects, as has been observed with

<sup>a</sup>School of Materials Science and Engineering, Tongji University, Shanghai 200092, PR China

<sup>b</sup>The Institute for Translational Nanomedicine, Shanghai East Hospital, the Institute for Biomedical Engineering & Nano Science, Tongji University School of Medicine, Shanghai 200092, PR China. E-mail: yilongwang@tongji.edu.cn, donglu.shi@uc.edu

<sup>c</sup>Department of Pathology, Wake Forest University School of Medicine, Winston-Salem, North Carolina, USA

<sup>d</sup>Department of Geological Sciences, Stanford University, Stanford, California, 94025, USA

<sup>e</sup>The Materials Science and Engineering Program, Dept. of Mechanical and Materials Engineering, College of Engineering and Applied Science, University of Cincinnati, Cincinnati, Ohio, 45221, USA

† Electronic supplementary information (ESI) available. See DOI: 10.1039/c6nr07161a

DOXIL, which can cause severe hand-foot syndrome.<sup>20</sup> Moreover, some biocompatible molecules or proteins, such as gamma-polyglutamic acid, hyaluronic acid, and lectin have been found to be possible targeting moieties through over-expressed biomarkers.<sup>21–23</sup>

To address these critical issues in biomarkers, research efforts have been devoted to searching for a universal characteristic of all types of cancer cells, regardless of their molecular and genomic differences.<sup>24</sup> The most consistent hallmark of cancer cells is the greatly increased level of glycolysis.<sup>25–27</sup> The levels of glucose uptake and lactate secretion can be up to thirty times greater than that of normal cells. We have recently found that the surfaces of twenty-two cancer cell lines are negatively-charged due to lactate secretion across the plasma membrane.<sup>24</sup> In a normal cell, mitochondria are described as “the powerhouse of cells” for generating most of the cell’s supply of adenosine triphosphate (ATP) by glycolysis and tricarboxylic acid cycle (TCA) consuming glucose. In a cancer cell, however, the metabolic pattern is entirely different. Due to the “Warburg Effect,” in cancer cells, the cross-membrane movement of lactate is an end product of the glycolysis pathway in hypoxia.<sup>25–27</sup> The loss of highly mobile lactate from the cytoplasm will inevitably remove labile inorganic cations, such as  $\text{Na}^+$  and  $\text{H}^+$ , to form lactate salts and acids as part of the lactate cycle. Thus, there would not be a buildup of lactate acids near the cancer cells that disrupt the downward gradient of lactate acids outwardly across the plasma membrane. When cancer cells continuously lose cations from the cytoplasm, generation of net negative charges on cell surfaces becomes inevitable. The high levels of glycolysis, consumption of glucose, and lactate secretion are the most distinctive hallmarks of cancer cell metabolism. These biochemical reactions are fundamentally responsible for the negative surface charge of cancer cells. The only mechanism by which a negative surface charge can be sustained is through the continuous movement of ions that can generate stable charges.<sup>28,29</sup> The highly elevated level of glycolysis results in the secretion of a large amount of lactate that provides a continuous source of mobile anions moving from the cell interior to its exterior. Thus, the high concentration of the negative surface charge is a unique characteristic of cancer cells.

If a surface-charged nanovector is functionalized with certain therapeutic means, cell killing can be directly accomplished upon its binding to the cancer cells *via* charge-mediated targeting. Recently, photothermal therapy using nanomaterials including gold nanoparticles, graphene oxide, magnetic nanoparticles, has been utilized as an ideal physical process for cancer cell ablation without any anticancer drugs.<sup>30–32</sup> This strategy has a direct therapeutic effect, but with low cytotoxicity as compared with conventional chemo or radiological therapies. Among several nanomaterials,  $\text{Fe}_3\text{O}_4$  nanoparticles have been shown to be a promising agent for photothermal therapy under near infrared irradiation (NIR).<sup>33</sup>

In this study, we designed fluorescent superparamagnetic  $\text{Fe}_3\text{O}_4$  composite nanoparticles with electrically charged surfaces for cancer cell biomarkerless targeting and photothermal

killing. The  $\text{Fe}_3\text{O}_4$  composite nanoparticles bind to the cancer cells entirely due to the opposite electrostatic charges. An NIR laser irradiation is subsequently applied to induce local photothermal hyperthermia for direct cancer cell ablation. Systematic *in vitro* experiments were carried out to investigate the surface charge-mediated targeting and photothermal ablation of HeLa cells, with two normal cell lines (HUVEC and L929 cells) as control. The same approach can certainly be applied to other cancer phenotypes as they share the common negatively-charged cell surfaces. Our experimental results indicate a high potential of electrical-charge-mediated, biomarkerless cell targeting and effective photothermal therapy.

## Results and discussion

### Design and synthesis of the surface-charged fluorescent superparamagnetic composite nanoparticles for charge-based cell targeting and direct photothermal annihilation

Fig. 1 shows the schematic pathway for preparation of the surface-charged magnetic composite nanoparticles, charge-based cell targeting and binding, and photothermal cell killing. As illustrated in Fig. 1A, the  $\text{Fe}_3\text{O}_4$  microspheres are synthesized through a solvothermal process. The magnetic nanoclusters are functionalized with polyacrylic acid (PAA). A thin layer of an amorphous silica shell is then applied as a coating in order to increase the affinity between the magnetic core and the fluorescent organosilane components and prevent the fluorescence from being quenched by the magnetic core. To introduce the fluorescence dye into the nanomaterials, the APTES (3-aminopropyltrimethoxysilane)–FITC complex is initially reacted, followed by grafting onto the

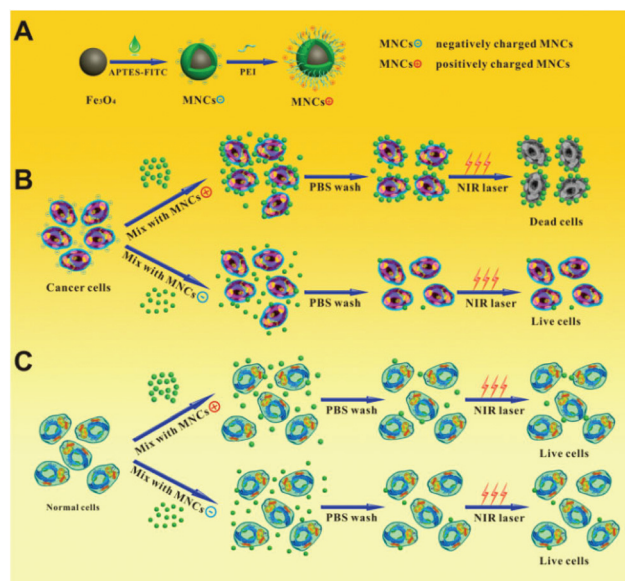


**Fig. 1** Pathway for preparation of the surface-charged, fluorescent, superparamagnetic composite nanoparticles and the procedure for electric charge-mediated cell targeting and photothermal therapy.

surface of the Fe<sub>3</sub>O<sub>4</sub>@silica composites through a typical sol-gel reaction. During the reaction, a portion of TEOS is added in the later stage in order to envelop the fluorescent layer. The product at this stage exhibits a strong negative surface charge due to the abundant presence of Si-OH. For positively-charged composite nanoparticles, PEI molecules are applied to modify their surfaces. The positively and negatively-charged composite nanoparticles are respectively denoted as MNCs $\oplus$  and MNCs $\ominus$ .

As shown in Fig. 1B, both MNCs $\oplus$  and MNCs $\ominus$  are incubated with the cancer cells at 4 °C for 5 min respectively, and the extra MNCs are washed away. A large amount of MNCs $\oplus$  is bound to cancer cells due to the opposite charges. As a result of the same charge sign, MNCs $\ominus$  are repelled by the cancer cells and washed away. Upon efficient cell targeting and binding by MNCs $\oplus$ , an 808 nm laser is used to induce photothermal heat. Due to the intimate contact between the MNCs $\oplus$  and cancer cells, the cancer cells are annihilated by the thermal pulse. In sharp contrast, there is an insignificant photothermal effect on the MNCs $\ominus$ , as the particles are mostly removed by washing. In the control experiments (Fig. 1C), the normal cells are treated with both MNCs $\oplus$  and MNCs $\ominus$  under the same conditions, respectively. Normal cells incubated with either MNCs $\oplus$  or MNCs $\ominus$  remain alive after NIR laser irradiation. Since these normal cells have neutral surfaces,<sup>24</sup> they are electrostatically nonreactive with either MNCs $\oplus$  or MNCs $\ominus$ . Consequently, both MNCs $\oplus$  and MNCs $\ominus$  are easily washed away.

Fig. 2 shows TEM and SEM images and physiochemical features of the magnetic composite nanoparticles. The average size of magnetic composite nanoparticles is 105 nm, determined by TEM and SEM as shown in Fig. 2A-C, respectively. The hydrodynamic size and size distribution are shown in Fig. 2D. The maximum sizes of the composite nanoparticles with the positive and negative charges are 125 and 113 nm,

respectively. The zeta potentials of the negatively and positively-charged MNCs are -18.0 mV and +35.6 mV, respectively (MNCs were dispersed in deionized water, pH 7.0). Fig. 2E shows the pH-zeta potential curves of the negatively and positively-charged composite nanoparticles. From these curves, one can see that the surface-charged MNCs are well dispersed in aqueous solution under neutral conditions through an electrostatic repulsion.

Fig. 2F shows the hysteresis loops of the magnetic composite nanoparticles with different surface charges. Both the positively (MNCs $\oplus$ ) and negatively (MNCs $\ominus$ )-charged MNCs are characteristically superparamagnetic with reversible hysteresis and saturated magnetization of 23 emu g<sup>-1</sup>. Note that the  $M_s$  value of MNCs is relatively low compared with the pure Fe<sub>3</sub>O<sub>4</sub> nanoparticles reported in the literature (around 75.6 emu g<sup>-1</sup>).<sup>34</sup> This decrease in  $M_s$  is associated with the composite nature that the MNCs contain fractions of the nonmagnetic components such as silica and polymer.<sup>35</sup> However, we found the Fe<sub>3</sub>O<sub>4</sub> composite nanoparticles highly efficient in generating photothermal heat for effective hyperthermia cell killing. As shown in this figure, both composites with opposite signs exhibit the same magnetization indicating that the magnetic properties are maintained after PEI surface modification. Similarly, both MNCs $\oplus$  and MNCs $\ominus$  show a strong green fluorescence when irradiated with blue light without any adverse effect of PEI surface functionalization (ESI Fig. S1A and B†).

### Photothermal properties of magnetic composite nanoparticles

The photothermal conversion efficiency,  $\eta$ , of MNCs was calculated using the formulations developed by Roper *et al.*<sup>36-38</sup> The photothermal conversion efficiency  $\eta$  can be expressed as (see the ESI† for the detailed calculations):

$$\eta = \frac{hS(T_{\text{Max}} - T_{\text{Surr}}) - Q_s}{I(1 - 10^{-A_{808}})} \quad (1)$$

where the proportionality constant  $h$  (mW (m<sup>2</sup> °C)<sup>-1</sup>) is the heat transfer coefficient;  $S$  (m<sup>2</sup>) is the surface area of the container; the value of  $hS$  is obtained from Fig. S2;  $T_{\text{Max}}$  (°C) is the system maximum temperature;  $T_{\text{Surr}}$  (°C) is the surrounding temperature;  $Q_s$  (mW) is the energy input due to the light absorption by the quartz sample cell and the solvent, which is measured independently to be 5 mW;  $I$  (2 W) is the incident laser power, and  $A_{808}$  is the absorbance of the MNCs in the quartz sample cell at the wavelength of 808 nm, whose value was determined to be 1.2513 in this study. Using the formulations (eqn (1)-(4)) in the ESI,† the photothermal conversion efficiency  $\eta$  is calculated to be 31.9%.

Fig. 3A and B show the heating curves of the aqueous solutions of the positively and negatively-charged composite nanoparticles at different concentrations. Under NIR laser irradiation (0.1 mL aqueous solution,  $\lambda = 808$  nm, 2 W cm<sup>-2</sup>) for 5 min the photothermal effect increased dramatically with the increased concentration. Within 5 min of irradiation, the temperature of the MNCs $\oplus$  aqueous solution at 0.15 mg mL<sup>-1</sup> rose to just above 55 °C. The temperature gap, after laser

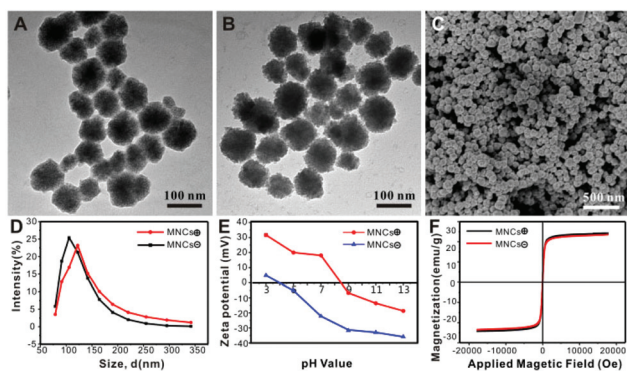


**Fig. 2** Physiochemical properties of the surface-charged magnetic composite nanoparticles (MNCs). Transmission electronic microscopy image of (A) positively-charged MNCs and (B) negatively-charged MNCs; (C) scanning electronic microscopy image of positively-charged MNCs; (D) dynamic light scattering size and distribution of the surface-charged MNCs; (E) pH-zeta potential curves of the positively and negatively-charged MNCs, and (F) hysteresis loops of the negatively and positively-charged MNCs.

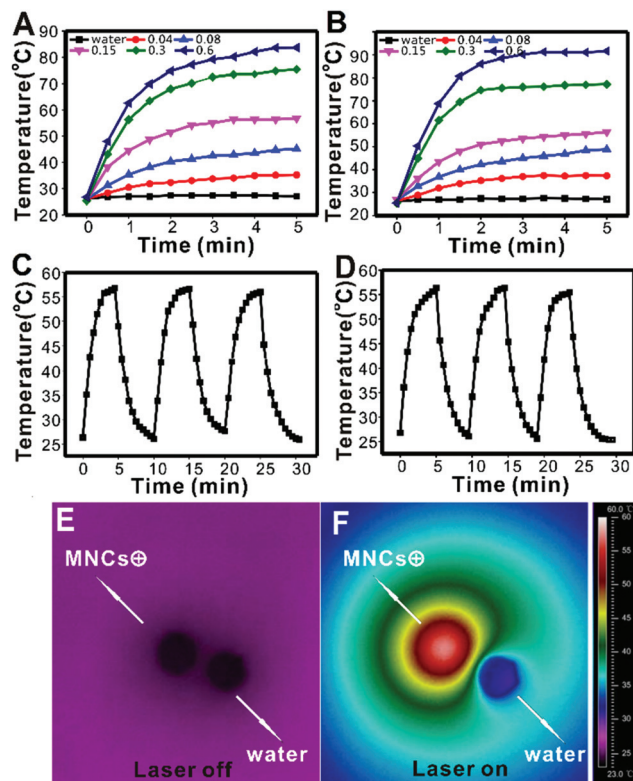


**Fig. 3** The photothermal properties of the surface-charged magnetic composite nanoparticles (MNCs), showing (A) the temperature profiles of pure water and aqueous dispersion of the positively-charged MNCs at different concentrations under 808 nm laser irradiation with a power density of  $2.0 \text{ W cm}^{-2}$ ; (B) the temperature profiles of pure water and aqueous dispersion of the negatively-charged MNCs under the same conditions; (C) the temperature vs. time curve for the positively-charged MNCs solutions ( $0.15 \text{ mg mL}^{-1}$ ) irradiated with an 808 nm laser ( $2 \text{ W cm}^{-2}$ ) for three on/off cycles (on: 5 min, off: 5 min); (D) the temperature vs. time curve for the negatively-charged MNC solutions for three on/off cycles under the same conditions; (E) the NIR thermal images of droplets containing the positively-charged MNCs and pure water on the glass slide with laser off, and (F) the NIR thermal images of the same droplets with laser on.

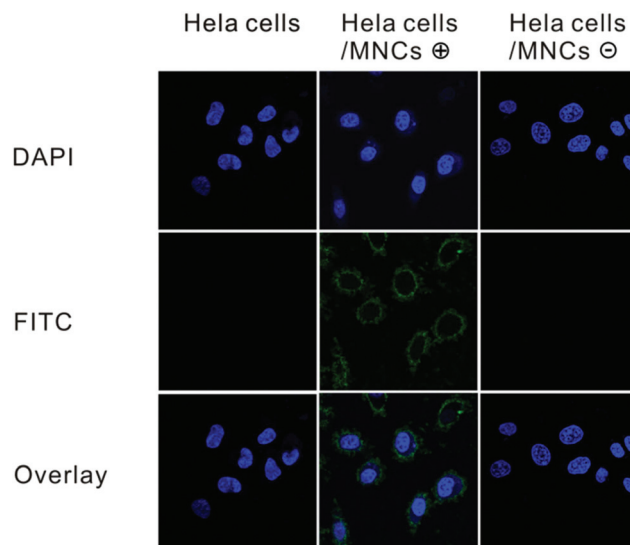
irradiation, between the MNC aqueous solution and the water control is more than  $30 \text{ }^\circ\text{C}$ . The negatively-charged magnetic composite nanoparticles exhibit a similar photothermal effect under NIR laser irradiation (Fig. 3B). The photothermal effects are both time and concentration-dependent. The photostabilities of the positively-charged and negatively-charged MNCs were tested by three cycles of laser exposure (Fig. 3C and D). Both the MNCs raised the temperature of the solution to the same level, which suggests that their good photostabilities allow repeated photothermal treatment.

Fig. 3E and F show the NIR thermal images of a droplet of the positively-charged MNCs aqueous solution and a droplet of the water blank on a glass slide. Fig. 3E shows the image with the NIR laser off, while the laser is on in Fig. 3F. As expected, the two droplets display the same low-temperature images without laser irradiation. After NIR laser irradiation for 5 min, the larger droplet with MNCs shows a much higher

temperature than the nearby droplet without MNCs. These images provide the direct evidence of a strong photothermal effect on the MNCs.

### Charge-based cancer cell targeting and binding by the positively-charged MNCs

It was reported that the cancer and non-cancerous cell surfaces exhibit significantly different lipid compositions. The presence of anionic lipids, such as phosphatidylserine, on the outer leaflet of the cancer cell membrane results in a negatively-charged cell surface,<sup>39</sup> whereas zwitterionic phospholipids and sphingomyelin occupy a large portion of the noncancerous cell membranes, making them either neutral or only slightly charged.<sup>40</sup> Therefore, the charge-based cancer cell targeting and binding by the positively-charged MNCs is the prerequisite for effective photothermal annihilation of cancer cells. In order to evaluate the specificity of the charge-based targeting and binding of the positively-charged MNCs, we analyzed the binding ability of different MNCs to both cancer cells and normal cells. HUVEC cells and L929 cells were chosen as the normal cell control. HeLa cancer cells or normal cells were used to interact with either the positively-charged or negatively-charged MNCs, respectively. Reducing the interaction time and incubation temperature is critical for promoting the electrostatic interaction by preventing endocytosis of composite nanoparticles by the cells.<sup>24</sup> After 5 min incubation of the MNCs with cells, the extra MNCs were removed by repeated washing with PBS solution. As shown in Fig. 4 and ESI Fig. S3,<sup>†</sup> the green fluorescence from the FITC dye embedded in MNCs is visible around the cancer cells (cell nucleus was stained with DAPI) treated with the positively-charged MNCs (ESI Fig. S1C and D<sup>†</sup>). In contrast, hardly any green



**Fig. 4** Comparison of fluorescence confocal images of the treated cancer cells (HeLa cells) with magnetic composite nanoparticles (MNCs) of different surface charges. DAPI is used to stain the cell nucleus. FITC is labeled in the positively-charged or negatively-charged MNCs.

fluorescence is observed on the membrane of the cancer cells treated with the negatively-charged MNCs or the normal cells treated with either the positively or negatively-charged MNCs. These results clearly indicate that the cancer cell surfaces are negatively-charged, and therefore largely bound to MNCs $\oplus$ . As for the normal cells, no cell binding takes place by either MNCs $\oplus$  or MNCs $\ominus$ , indicating that they are either neutral or weakly charged.<sup>40</sup> Additional experimental results with different parameters (ESI Fig. S4 $\dagger$ ), indicate the temperature-independent electrostatic interactions between the positively-charged composite nanoparticles and various cells studied. Based on these results, we conclude that cell targeting *via* surface charge is a highly effective strategy regardless of the phenotype of the cancer cells.

In addition to fluorescence images, we conducted flow cytometry after incubation of the HeLa cells with MNCs $\oplus$  and MNCs $\ominus$ , respectively. The blank HeLa cells were used as a control. ESI Fig. S5 $\dagger$  shows that, compared with the background noise of the control, only the HeLa cells that have been incubated with MNCs $\oplus$  have an enhanced fluorescent signal owing to the embedded FITC dye. SEM was also used to investigate the electrostatic interactions between the MNCs and various cells. The left column images of Fig. 5 show the morphologies of the pure cancer cells and normal cells as the control. The middle column shows the images of three different kinds of cells incubated with the positively-charged MNCs. The corresponding images of the cells with negatively-charged MNCs are shown in the right column. Almost all of the cancer cells are intimately surrounded by a high concentration of MNCs $\oplus$ . Under the same incubation conditions, hardly any negatively-charged MNCs remain after the washing procedure. No charged MNCs are visible on the surface of the

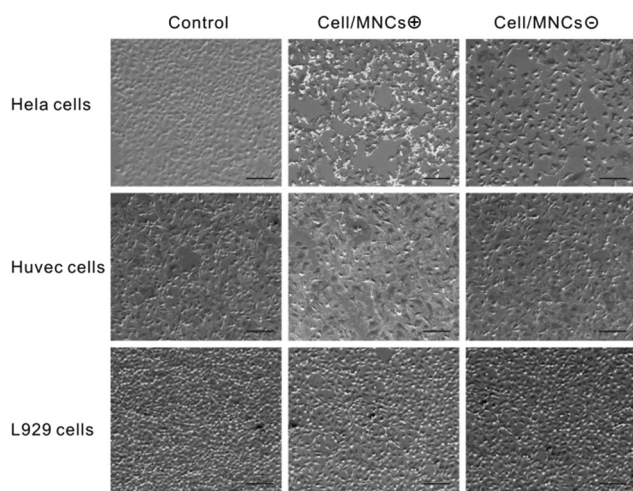


**Fig. 5** SEM images of the treated cancer cells (HeLa) and normal cells (L929 and Huvec) with magnetic composite nanoparticles (MNCs) of different surface charges. The left column is the cell control. The middle column represents the cells with positively-charged MNCs (MNCs $\oplus$ ). The right column shows the cells with negatively-charged MNCs (MNCs $\ominus$ ). The scale bar represents 100  $\mu\text{m}$ .

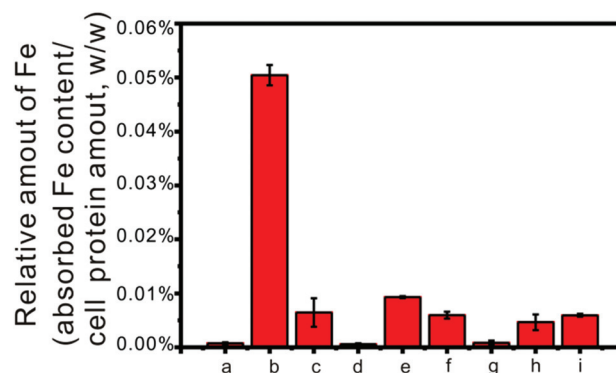


**Fig. 6** Relative amount of Fe of magnetic composite nanoparticles (MNCs) adhered onto the surfaces of different cells as indicated, measured by ICP-AES analysis in terms of elemental Fe per mass of cell protein. (a) Blank HeLa cells; (b) HeLa cells with positively-charged MNCs (MNCs $\oplus$ ); (c) HeLa cells with negatively-charged MNCs (MNCs $\ominus$ ); (d) blank Huvec cells; (e) Huvec cells with MNCs $\oplus$ ; (f) Huvec cells with MNCs $\ominus$ ; (g) blank L929 cells; (h) L929 cells with MNCs $\oplus$ , and (i) L929 cells with MNCs $\ominus$ .

normal cells after incubation with either the positively-charged or the negatively-charged MNCs. The SEM micrographs of the different cell types that have interacted with MNCs $\oplus$  are shown at a higher resolution in ESI Fig. S6 $\dagger$ . The SEM images provide further evidence of cell targeting and binding based on opposite surface charges between the MNCs and the cancer cells.

For quantitative evaluation of selective cell binding, ICP-AES analyses of the Fe element was completed in order to determine the amount of the adsorbed MNCs on the cancer or the normal cell membrane. Fig. 6 shows the amount of iron present on the different cell types. The Fe concentration is calculated based on the amount of Fe adsorbed per cell protein mass. The ratio of the positively-charged MNCs bound to the cancer cells is significantly higher than the negatively-charged MNC counterpart, or the positively-charged MNCs bound with the normal cells. These ICP-AES quantitative results are consistent with SEM and fluorescence images. All experimental results clearly show selective electrostatic cancer cell targeting and binding by the positively charged MNCs. Upon subsequent NIR irradiation, cancer cells, largely bound to the positive MNCs, are effectively annihilated by the strong photothermal effect on Fe<sub>3</sub>O<sub>4</sub>.

### Surface charge-mediated photothermal annihilation of cancer cells by the positively-charged MNCs

*In vitro* cell cytotoxicity of MNCs was completed with different particle surface charges against the cancer cell line HeLa and two reference normal cell lines L929 and HUVEC, under the same photothermal conditions. The MNCs of different concentrations were added to each group (three wells) for a given period. The cytotoxicities of the positively and negatively-charged MNCs against cancer cells or normal cells were measured using the CCK-8 assay. Incubation time was kept

relatively short (5 min) at a low temperature of 4 °C in order to retard endocytosis of composite nanoparticles by cells *via* a vesicular transport pathway. This is to ensure the sufficient electrostatic interaction between the cells and composite nanoparticles for both cancer cell targeting and subsequent photothermal treatment. To investigate the original cytotoxicity of MNCs, the composite nanoparticles were incubated with cells for 30 min without laser irradiation. Upon incubation before NIR laser irradiation, the unattached MNCs in the DMEM were washed three times with PBS. Note that effective photothermal annihilation results from the intimate contact of MNCs with the cancer cells due to the attraction of opposite surface charges. As described earlier, a washing procedure was applied after cell binding, assuring only those interfaced with the cancer cells participate in the photothermal process. However, most of the previous photothermal therapeutic studies did not employ this procedure, therefore relying upon only the average solution temperature rise without considering the particle spatial distribution and particle per cell interface contacts.

Fig. 7A shows the viabilities of different cells at different concentrations. As shown in this figure, for HeLa cells, the positively and negatively-charged MNCs exhibit similar cytotoxicities without laser irradiation at a concentration of 0.15 mg mL<sup>-1</sup>. However, with laser irradiation, the positively-charged MNCs result in a strong photothermal cancer cell killing effect at this concentration. In sharp contrast, there is a negligible annihilation effect of the negatively-charged MNCs as compared with their pure composite nanoparticle counterparts. The photothermal cell killing is considerably enhanced at higher concentrations of MNCs<sup>+</sup> as compared with MNCs<sup>-</sup> under laser irradiation or pure MNCs without irradiation. These results clearly show charge-based cell targeting and effective cancer cell annihilation by MNCs only with the positive surface charges. For the normal cells, insignificant cell targeting and annihilation was observed with the positively-charged MNCs indicating that they are electrically neutral. However, slight differences were observed between the L929 and HUVEC cells. With laser irradiation, both positively-

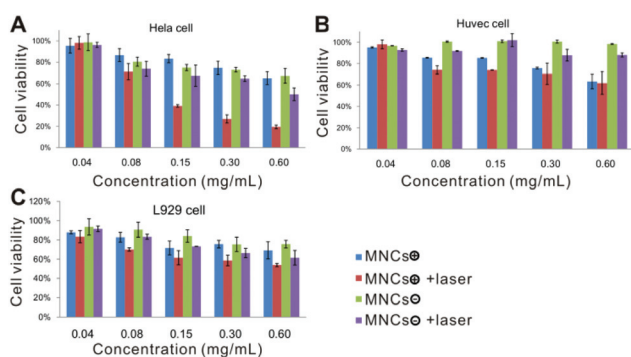


**Fig. 7** Cell viability vs. concentration of surface-charged magnetic composite nanoparticles for HeLa, Huvec, and L929 cells under different treatments. MNCs<sup>+</sup> refers to positively-charged MNCs, MNCs<sup>-</sup> refers to negatively-charged MNCs.

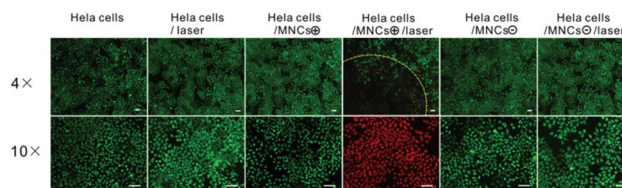


**Fig. 8** *In vitro* photothermal therapy effect of different kind of surface-charged magnetic composite nanoparticles (MNCs) on the HeLa cell with or without laser irradiation; live-dead staining of HeLa cells by AM/PI. Cells are incubated with MNCs at a concentration of 0.15 mg mL<sup>-1</sup> for 5 min and irradiated using an 808 nm laser for 10 min with a power density of 2 W cm<sup>-2</sup>. The scale bars are 100 μm in both fields.

charged and negatively-charged MNCs show a mild annihilation of L929 cells as compared with their pure composite nanoparticle counterpart.

Fig. 8 shows the fluorescence images of the cells with live-dead staining. Under the same conditions, only HeLa cells treated with the positively-charged MNCs with laser irradiation show a red fluorescence signal, which means that most of the HeLa cells were killed by the photothermal effect, mediated by the surface charge. No dead cells were observed for the blank cells, the cells with laser, and the cells with MNCs without laser. The infrared thermal camera was used to monitor the temperature in each well. It was found that the temperature was the highest in the well containing HeLa cells which adhered to the positively-charged MNCs. However, in other wells, although the same concentration of MNCs was used, few of the MNCs remained after several washings due to weak cell-particle interaction. As a result, the normal cells exhibit high viability under NIR irradiation (ESI Fig. S7†). These photothermal treatment results provide strong evidence for effective electrostatic charge-based targeting and direct photothermal cancer cell annihilation.

## Conclusions

We have developed a charge-mediated cancer cell targeting and killing strategy that does not rely on any biomarkers and anticancer drugs. Cell targeting is achieved based on a hallmark characteristic of all cancer cells: the negatively-charged cell surfaces. The lactate-secretion-generated negative surface charge is a biophysical characteristic common to all cancer cells, which is regulated by cellular glycolysis. The negative surface charges can be utilized for cell targeting regardless of their genomic differences and cancer phenotypes; thus avoiding the inherent complexity in using the conventional biomarkers. Fluorescent superparamagnetic Fe<sub>3</sub>O<sub>4</sub> composite nanoparticles have been designed with the altered surface electrical charge sign for both cell targeting and direct photothermal cancer cell killing. By manipulating the charge sign of the composite nanoparticles, we have investigated several cell lines including HeLa and normal cells. Using this unique surface-charged nano-probe, the cancer cells are shown to be

negatively-charged, consistent with our previous study.<sup>24</sup> The positively-charged composite nanoparticles selectively bind onto HeLa cells due to opposite charges. The intimate contacts between the positive nanoparticles and the negative cancer cells enable direct and effective annihilation of the cancer cells upon laser irradiation induced photothermal hyperthermia. In sharp contrast, no significant binding on cancer cells takes place with the negatively-charged composite nanoparticles due to the repulsive force between them, therefore resulting in insufficient cell killing. The normal cells are found to be electrostatically unresponsive to the nanoparticles with either positive or negative charges, indicating that they are essentially neutral.

## Experimental

### Materials

Iron(III) chloride hydrate ( $\text{FeCl}_3 \cdot 6\text{H}_2\text{O}$ ), ethylene glycol, sodium acetate, ammonium hydroxide ( $\text{NH}_4\text{OH}$ , 28 wt%), and hydrochloric acid (37 wt% aqueous solution) were purchased from Shanghai (China) Reagent Company. Tetraethyl orthosilicate (TEOS), (3-aminopropyl) triethoxysilane (APTES) and fluorescein isothiocyanate (FITC) were purchased from Sigma-Aldrich (USA). Branched poly(ethylene imine) (PEI, 99%,  $M_w = 10\,000$ ) was purchased from Alfa Aesar. Deionized water (DIW, 18.2 M $\Omega$  cm resistivity at 25 °C) was made by using a Thermo Easypure II UF System throughout the entire experiment.

### Cell culture materials

RPMI-1640 medium, heat-inactivated fetal bovine serum, penicillin–streptomycin and 0.25% trypsin-EDTA were purchased from Gibco Corp. Dulbecco's Modified Eagle's medium (DMEM) and phosphate-buffered saline (PBS) were purchased from Hyclone Corp. The rest of the media for cell culture was purchased from Corning Corp.

### Syntheses of surface-charged magnetic composite nanoparticles (MNCs)

Magnetic microsphere cores were prepared *via* a solvothermal reaction. 0.081 g of  $\text{FeCl}_3 \cdot 6\text{H}_2\text{O}$  was first dissolved in 30 mL of ethylene glycol under magnetic stirring. Subsequently, 0.3 g of polyacrylic acid (PAA) and 1.8 g urea were added to this solution. After being stirred for 0.5 h, the solution was heated at 200 °C for 12 h by using a Teflon-lined stainless-steel autoclave. When cooled to room temperature, a black product, namely  $\text{Fe}_3\text{O}_4$  microspheres, was collected with the help of a magnet. Followed by washing with ethanol and distilled water each three times, the  $\text{Fe}_3\text{O}_4$  microspheres were treated in a 0.15 M HCl aqueous solution under sonication for 15 min and washed to neutral. They were coated with silica *via* hydrolysis and condensation of tetraethyl orthosilicate (TEOS).

To prepare the negatively-charged MNC embedded fluorescence dye, the APTES–FITC complex was reacted under dark conditions overnight in ethanol. The complex was then grafted to the microspheres through reaction between APTES and hydroxyl groups on the  $\text{Fe}_3\text{O}_4@ \text{SiO}_2$  microsphere in the

mixture of ethanol and DI water with  $\text{NH}_4\text{OH}$  (v/v = 70/30). 30  $\mu\text{L}$  of TEOS was added 4 hours after APTES–FITC complex addition into the reaction system to ensure the negatively-charged surface of the microspheres. The reaction lasted for another 20 h in the dark. After washing, the negatively-charged fluorescent magnetic microspheres ( $\text{MNCs}^-$ ) were prepared. The positively-charged magnetic composite nanoparticles ( $\text{MNCs}^+$ ) were synthesized by surface modification of the negatively-charged MNCs with the polycation polymer PEI.

### Characterization of MNCs

Dynamic light scattering (DLS) measurement was carried out at 298.0 K with a Zetasizer Nano-ZS (Malvern, UK) equipped with a standard 633 nm laser. Transmission electron microscopy (JEM-2010) and scanning electron microscopy (JEOL S4800) were used to observe the composite nanoparticles. Magnetic characterization was carried out with a vibrating sample magnetometer (VSM, LakeShore 7407, USA) at 300 K. To investigate the photothermal properties of the MNCs, samples with a volume of 200  $\mu\text{L}$  were deposited into wells of a 48-well cell culture plate. The wells were irradiated with an 808 nm NIR laser (Ainajie Optoelectronics Technology, Beijing, China; fluence: 2 W  $\text{cm}^{-2}$ , spot size: 5 mm). Pre- and post-illumination temperature and images were taken by using a thermocouple and an infrared thermal camera (IRS/S6, Baifa Technology company, Shanghai, China).

### Cell lines and culture conditions

HeLa cells (Human Cervical Cancer Cells) and L929 cells (NCTC clone 929, mouse fibroblast) were cultured in Dulbecco's modified Eagle's medium (DMEM). The HUVEC cells (HUVEC, Human Umbilical Vein Endothelial Cells) were cultured in RPMI 1640 medium. Both were supplemented with 10% fetal bovine serum (FBS) and 1% penicillin–streptomycin. All the cells were maintained in a humidified atmosphere containing 5%  $\text{CO}_2$  at 37 °C. Depending on the purpose of the experiment, the cells were seeded on 6-well plates and 24-well plates, 96-well plates, a confocal dish or 25  $\text{cm}^2$  flasks. All sterile plastics were sourced from Corning.

Non-tumorigenic cell lines HUVEC and L929 were used as control in some experiments. Cell lines used in this study were obtained from the Chinese Academy of Sciences Cells Bank, Shanghai, China.

### Confocal microscopy imaging

HeLa cells, L929 cells and HUVEC cells were plated on a confocal dish for 24 h for cell targeting investigation. Upon incubation with composite nanoparticles (0.15 mg  $\text{mL}^{-1}$ ) for 5 min at 4 °C, the culture medium was removed and the samples were washed three times with PBS (pH 7.4) to remove the extra MNCs. The cell nucleus was stained with DAPI (4',6-diamidino-2-phenylindole, blue), and the composite nanoparticles were embodied with FITC (fluorescein isothiocyanate, green). The cells and composite nanoparticles were observed and analyzed under a Leica TCS SP5 confocal microscope (Leica, Germany).

### **In vitro cytotoxicity assays**

Cytotoxicity was assessed by using the Cell Counting Kit (CCK-8, Keygentec) The cells were seeded on 96-well plates and incubated for 30 min. After incubation with the composite nanoparticles for 30 min, 10  $\mu\text{L}$  CCK-8 was added to each 96-well dish and the cells were treated for 3 h. The assay absorbance was measured at a wavelength of 450 nm in a Microplate Reader. Cell survival was expressed as the percentage of absorption of the treated cells in comparison with that of the control cells.

### **Flow cytometry analysis**

The cells were seeded onto 6-well plates and grown for 24 h in DMEM (Hela cells) medium containing 10% FBS. 0.15 mg  $\text{mL}^{-1}$  MNCs with both positive and negative charges was added and incubated at 4  $^{\circ}\text{C}$  for 5 min respectively. The cells were subsequently rinsed three times with ice-cold PBS. The cells were digested with trypsin enzyme and transferred to tubes. Cell-associated fluorescence was determined using a BD FACS flow cytometer. In parallel, samples of the cells were collected by centrifugation.

### **Calculation of the photothermal conversion efficiency**

The photothermal conversion efficiency,  $\eta$ , of MNCs was calculated using the formulations (eqn (1)–(4)†) developed by Roper *et al.*<sup>36–38</sup>

### **Photothermal toxicity measurements for cells**

The CCK-8 assay was adopted to evaluate the photothermal therapy effect of MNCs. HeLa, HUVEC and L929 cells in logarithmic growth were cultured in 96-well plates for 24 h, and then incubated with the positively-charged MNCs (MNCs $\oplus$ ) and the negatively-charged MNCs (MNCs $\ominus$ ) at 4  $^{\circ}\text{C}$  for 5 min. Excess NPs were removed by cold PBS washing. After that, the cells were irradiated with an 808 nm laser with a power density of 2  $\text{W cm}^{-2}$  for 10 min. The viabilities of HeLa cells, and two normal HUVEC and L929 cells, as control cell lines, were determined after irradiation with an 808 nm laser.

### **Calcein-AM/PI assay**

After HeLa cells were incubated with MNCs for 5 min, excess MNCs were removed by PBS washing. The 808 nm laser was then applied for 10 min. For calcein-AM/PI assay staining, the cells were co-stained with a solution mixture containing calcein-AM (2  $\text{mmol L}^{-1}$ ) and PI (8  $\text{mmol L}^{-1}$ ). The live/dead cells labeled in green/red colors were examined using a fluorescence microscope. Calcein-AM and PI were excited with the 488 nm and 533 nm lasers respectively.

### **ICP-AES analysis**

After the charged MNCs were incubated with the cells, the excess MNCs were washed away. The amount of the remaining MNCs on the surface of the cells was characterized by inductively coupled plasma atomic emission spectrometry (ICP-AES). For each sample, three duplicates were analyzed.

### **Scanning electron microscopy characterization of cells-MNCs binding**

The cells were seeded on cell slides in a 24-well plate and cultured under standard conditions. When the cells achieved confluence, they were incubated with 1 mL of 0.15 mg  $\text{mL}^{-1}$  composite nanoparticles. Blank cells as control were cultured in medium without composite nanoparticles. After incubation, the cells were washed twice with PBS. After removing excess PBS, the cells were immediately fixed in glutaraldehyde at 4  $^{\circ}\text{C}$  for 24 h. Then, the samples were dehydrated in 50%, 75%, and 100% series of graded alcohol solutions and dried. Dry cellular constructs were sputtered with gold and observed by scanning electron microscopy (SEM).

## **Acknowledgements**

This work was supported by grants from the National Natural Science Foundation of China (31571018), the Science and Technology Commission of Shanghai Municipality (15ZR1443200, 15441905900). The author DS from the University of Cincinnati is partially supported by a National Science Foundation grant EEC-1343568.

## **Notes and references**

- 1 X. Gao, Y. Cui, R. M. Levenson, L. W. Chung and S. Nie, *Nat. Biotechnol.*, 2004, **22**, 969–976.
- 2 I. Brigger, C. Dubernet and P. Couvreur, *Adv. Drug Delivery Rev.*, 2002, **54**, 631–651.
- 3 M. Ferrari, *Nat. Rev. Cancer*, 2005, **5**, 161–171.
- 4 C. M. Cobley, J. Chen, E. C. Cho, L. V. Wang and Y. Xia, *Chem. Soc. Rev.*, 2011, **40**, 44–56.
- 5 Y. Wang and H. Gu, *Adv. Mater.*, 2015, **27**, 576–585.
- 6 E.-Q. Song, J. Hu, C.-Y. Wen, Z.-Q. Tian, X. Yu, Z.-L. Zhang, Y.-B. Shi and D.-W. Pang, *ACS Nano*, 2011, **5**, 761–770.
- 7 A. Accardo, D. Tesaro and G. Morelli, *Polym. J.*, 2013, **45**, 481–493.
- 8 L. Rajendran, H.-J. Knölker and K. Simons, *Nat. Rev. Drug Discovery*, 2010, **9**, 29–42.
- 9 Y. Yan, G. K. Such, A. P. Johnston, J. P. Best and F. Caruso, *ACS Nano*, 2012, **6**, 3663–3669.
- 10 L. Cerchia and V. De Franciscis, *Trends Biotechnol.*, 2010, **28**, 517–525.
- 11 L. M. Weiner, R. Surana and S. Wang, *Nat. Rev. Immunol.*, 2010, **10**, 317–327.
- 12 S. Tapaneeyakorn, W. Chantima, C. Thepthai and T. Dharakul, *Biochem. Biophys. Res. Commun.*, 2016, **475**, 149–153.
- 13 L. Geng, Z. Wang, X. Jia, Q. Han, Z. Xiang, D. Li, X. Yang, D. Zhang, X. Bu, W. Wang, Z. Hu and Q. Fang, *Theranostics*, 2016, **6**, 1261–1273.
- 14 H.-S. Cho, Z. Dong, G. M. Pauletti, J. Zhang, H. Xu, H. Gu, L. Wang, R. C. Ewing, C. Huth, F. Wang and D. Shi, *ACS Nano*, 2010, **4**, 5398–5404.

- 15 S.-M. Lee, H. Chen, T. V. O'Halloran and S. T. Nguyen, *J. Am. Chem. Soc.*, 2009, **131**, 9311–9320.
- 16 M. E. Davis, J. E. Zuckerman, C. H. J. Choi, D. Seligson, A. Tolcher, C. A. Alabi, Y. Yen, J. D. Heidel and A. Ribas, *Nature*, 2010, **464**, 1067–1070.
- 17 R. K. Jain and T. Stylianopoulos, *Nat. Rev. Clin. Oncol.*, 2010, **7**, 653–664.
- 18 C. Liang, X. Song, Q. Chen, T. Liu, G. Song, R. Peng and Z. Liu, *Small*, 2015, **11**, 4856–4863.
- 19 G. Mikhaylov, U. Mikac, A. A. Magaeva, V. I. Itin, E. P. Naiden, I. Psakhye, L. Babes, T. Reinheckel, C. Peters and R. Zeiser, *Nat. Nanotechnol.*, 2011, **6**, 594–602.
- 20 D. Lorusso, A. Di Stefano, V. Carone, A. Fagotti, S. Pisconti and G. Scambia, *Ann. Oncol.*, 2007, **18**, 1159–1164.
- 21 T. Kurosaki, T. Kitahara, S. Kawakami, Y. Higuchi, A. Yamaguchi, H. Nakagawa, Y. Kodama, T. Hamamoto, M. Hashida and H. Sasaki, *J. Controlled Release*, 2010, **142**, 404–410.
- 22 E. J. Oh, K. Park, K. S. Kim, J. Kim, J.-A. Yang, J.-H. Kong, M. Y. Lee, A. S. Hoffman and S. K. Hahn, *J. Controlled Release*, 2010, **141**, 2–12.
- 23 J. Li, X. Qu, G. F. Payne, C. Zhang, Y. Zhang, J. Li, J. Ren, H. Hong and C. Liu, *Adv. Funct. Mater.*, 2015, **25**, 1404–1417.
- 24 B. Chen, W. Le, Y. Wang, Z. Li, D. Wang, L. Ren, L. Lin, S. Cui, J. J. Hu, Y. Hu, P. Yang, R. C. Ewing, D. Shi and Z. Cui, *Theranostics*, 2016, **6**, 1887–1898.
- 25 M. G. Vander Heiden, L. C. Cantley and C. B. Thompson, *science*, 2009, **324**, 1029–1033.
- 26 P. P. Hsu and D. M. Sabatini, *Cell*, 2008, **134**, 703–707.
- 27 W. H. Koppenol, P. L. Bounds and C. V. Dang, *Nat. Rev. Cancer*, 2011, **11**, 325–337.
- 28 E. Blanco, H. Shen and M. Ferrari, *Nat. Biotechnol.*, 2015, **33**, 941–951.
- 29 C. C. Fleischer and C. K. Payne, *Acc. Chem. Res.*, 2014, **47**, 2651–2659.
- 30 L. Zou, H. Wang, B. He, L. Zeng, T. Tan, H. Cao, X. He, Z. Zhang, S. Guo and Y. Li, *Theranostics*, 2016, **6**, 762–772.
- 31 X. Yang, M. Yang, B. Pang, M. Vara and Y. Xia, *Chem. Rev.*, 2015, **115**, 10410–10488.
- 32 S. Shen, S. Wang, R. Zheng, X. Zhu, X. Jiang, D. Fu and W. Yang, *Biomaterials*, 2015, **39**, 67–74.
- 33 D. Shi, M. Sadat, A. W. Dunn and D. B. Mast, *Nanoscale*, 2015, **7**, 8209–8232.
- 34 L. Wang, J. Bai, Y. Li and Y. Huang, *Angew. Chem., Int. Ed.*, 2008, **47**, 2439–2442.
- 35 Q. W. Tian, J. Q. Hu, Y. H. Zhu, R. J. Zou, Z. G. Chen, S. P. Yang, R. W. Li, Q. Q. Su, Y. Han and X. G. Liu, *J. Am. Chem. Soc.*, 2013, **135**, 8571–8577.
- 36 D. K. Roper, W. Ahn and M. Hoepfner, *J. Phys. Chem. C*, 2007, **111**, 3636–3641.
- 37 Q. Tian, F. Jiang, R. Zou, Q. Liu, Z. Chen, M. Zhu, S. Yang, J. Wang, J. Wang and J. Hu, *ACS Nano*, 2011, **5**, 9761–9771.
- 38 M. E. Sadat, M. Kaveh Baghbador, A. W. Dunn, H. P. Wagner, R. C. Ewing, J. Zhang, H. Xu, G. M. Pauletti, D. B. Mast and D. Shi, *Appl. Phys. Lett.*, 2014, **105**, 091903.
- 39 S. Riedl, D. Zwegtack and K. Lohner, *Chem. Phys. Lipids*, 2011, **164**, 766–781.
- 40 E. M. Bevers, P. Comfurius and R. F. A. Zwaal, *Lupus*, 1996, **5**, 480–487.